Data-Driven Analysis of Zinc Stannate Nanostructured Thin Films for Gas Sensing Applications

Karrar Saad. Mohammed[1], Jasim Mohammed Mansoor[1], Asaad Ahmed Kamil[1], Nabeel Ali Bakr[1], Tahseen Hussein Mubarak[1], Sorina Iftimie[2] and Oana Brincoveanu[3]

[1]*Department of Physics, University of Diyala, 32001 Baqubah, Iraq,*

[2]*Faculty of Physics, University of Bucharest, Atomistilor Str. 405, 077125 Măgurele, Romania*

[3]*National Institute for Research and Development in Microtechnologie, Erou Iancu Nicolae Str. 126A, 077125 Bucharest, Romania*

{Alzanganaweesciphydr222301,Prof.asaad,prof.dr.tahseen}@uodiyala.edu.iq, nabeelalibakr@yahoo.com, sorina.iftimie@unibuc.ro, oana.brincoveanu@imt.ro

Keywords: ZnSnO3, Thin Films, Sol-Gel, XPS, Halder-Wagner, RT Gas Sensitivity.

Abstract: This study employs Sol-gel spin coating technique to synthesize ZnSnO3 nanostructured thin films on quartz substrates, intended for application as gas sensors to H2S, NO2, and NH3. The films were optimized by adjusting the ZnO:SnO_2 ratio. A variety of characterization techniques are conducted to calculate the structural, optical, electrical, and sensing characteristics of the synthesized thin films. XRD and Raman spectroscopy confirmed that an increase in Zn (wt%) content relative to Sn (wt%) content results in a phase transition from tetragonal rutile to hexagonal ilmenite phases. XPS and EDS analyses showed the anticipated oxidation states of Sn4+, Zn2+, and O2−, demonstrating the existence of oxygen vacancy defects. AFM with FE-SEM imaging revealed the existence of rough, spherical nanostructures that enhance surface area. Optical investigations revealed band gaps ranging from 3.3 to 3.6 eV. Hall effect measurements revealed a notable increase in electrical conductivity, rising from 1.97 (Ω cm)-1 to 3.37 (Ω cm)-1, which was associated with improved sensing performance. The films exhibited sensitivities of 42.2% for NO2, 22.4% for H2S, and 21.4% for NH3 at room temperature, with corresponding response times of 27s, 19.8s, and 26s, respectively. At 100°C, sensitivities were recorded at 75.3% for NO2, 27.3% for H2S, and 13.1% for NH3, with corresponding response times of 25.2s, 16.2s, and 20.7s, respectively. The maximum sensitivity was recorded at 200°C, with the films demonstrating 75.6% for NO2, 36.8% for H2S, and 10.1% for NH3. The corresponding response times were 17.1s for NO2, 17.1s for H2S, and 25.2s for NH3, with detection limits of 81 (ppm) for NO2, 13 (ppm) for H2S, and 11 (ppm) for NH3. The findings suggest that porous ZnSnO3 thin films are viable options for hazardous gas detection.

1 INTRODUCTION

Zinc stannate ($ZnSnO_3$) is a noteworthy oxide compound that has garnered considerable interest in materials science owing to its distinctive qualities, including high-sensitivity, enormous specifically surface area, non-toxic characteristics, and excellent compatibility. Moreover, regarding its structure and characteristics, it represents the most attractive group of nanoparticles. The chemical stability of ZnSnO3 under standard circumstances enhances its utility across multiple domains. Its promise as a luminous and photovoltaic material, as well as its applications in battery packs, batteries, solar energy cells, biosensors, gas detectors, and catalysts of all kinds have been thoroughly investigated to date. The effective storage capacity of $ZnSnO_3$ renders it a suitable choice for energy storage and smart system development [1]. The rapid increase in atmospheric concentrations of harmful gases, including NO_2, H_2S, NH3, CO_2, and volatile organic compounds, is largely attributable to the ongoing industrialization process [2]. The atmospheric reactions that produce organic nitrates and nitric acid, which are components of acid rain, rely on nitrogen dioxide (NO_2), a major pollutant emitted by vehicles and household appliances. Therefore, to preserve the environment and conduct continuous emission monitoring, it is crucial to design NO_2 sensors that are both accurate and selective. Hydrogen sulfide (H_2S) and ammonia

(NH3) are extremely hazardous gases that are generated in confined areas, such as sewage systems. These gases are byproducts of various industrial processes, including the gasification of coal, waste treatment, and petroleum refining. Due to the dangers they pose to both humans and the environment, detecting H_2S and NH_3 is of the utmost importance [3]. Gas sensors, especially those built on MOS technology, offer a potential solution to identifying these and other hazardous gases. The conductivity or resistivity of a material can be changed when gases react with metal oxide layers on its surface, changing the concentration of charge carriers at its core, gas sensing is this interaction [4]. The use of semiconductors like ZnO and SnO2 in metal-oxide-based sensors has recently been demonstrated to have effective gas detection capabilities, according to recent studies [5]-[7]. To detect minute gas concentrations in complex settings, it is essential to make these sensors more sensitive and selective [8], [9]. It is possible to greatly enhance the performance of MOS sensors by adding certain dopants to the semiconductor lattice. In the presence of multiple gases, it is especially challenging to obtain reliable readings with current gas detection systems that rely on human senses. Challenges with sensitivity and selectivity are also encountered by conventional sensors when monitoring complicated gas mixes. Hence, it is crucial to protect human health and the environment by creating novel materials that can detect gases at low concentrations and at lower temperatures. Ideal candidates for this purpose are nanostructured semiconducting materials, which have adjustable characteristics and increased surface to volume ratios [10], [11]. An extensive study has been conducted on the gas-sensing capabilities of various metal oxides, including ZnO [12], TiO_2 [13], SnO_2 [14], WO_3 [15], CuO [16], and NiO [17]. Energy consumption rises and safety issues multiply when these materials are subjected to high operating temperatures. Sensor performance has been greatly enhanced, enabling detection at lower temperatures, thanks to recent advancements such as the creation of doped, co-doped, and nanocomposite metal oxides. By enhancing the mobility of charge carriers and increasing the sensor's sensitivity to both oxidizing and reducing gases, heterojunction interfaces between multiple semiconductor materials also improve gas sensing [8], [10], [18]. Sol gel spin coating method has gained popularity for producing thin films due to its adaptability, cost-effectiveness, and control over film characteristics [19]. We examine the production of binary ZnO:SnO_2 thin films and evaluate the impact of different ZnO:SnO_2 weight ratios on the gas-sensing, surface-optical, electrical, and structural properties of the films. Our main areas of interest include the detection of NH_3, NO_2, and H_2S. In addition to being dangerous to humans, these gases exacerbate urban air pollution, which in turn causes a host of health problems, including respiratory illnesses. In this research, we use the sol-gel spin-coating technique to create binary thin films of ZnO and SnO2. The films' homogeneity, thickness, and composition may be precisely controlled using this method, which is crucial for their gas-sensing function. We intend to study the effect of mixing wt|% ratios on the electrical, optical, and structural characteristics of the films by changing the weight percentages of ZnO and SnO_2. In addition, we test the films at 30 ºC, 100°C, and 200°C to see how well they detect NO_2, H_2S, and NH_3. We aim to enhance gas sensor efficiency and cost-effectiveness by increasing sensor sensitivity while reducing operating temperature requirements.

2 EXPERMINANTEL PROCEDURE

Zinc Stannate (ZnSnO3) thin films were deposited on quartz substrates through the sol-gel spin coating utilizing an Ossila spin coater. The precursor solutions were formulated by dissolving 0.5M zinc acetate dihydrate ($Zn(CH_3COO)_2.\cdot 2H_2O$) and stannous chloride dihydrate ($SnCl_2\cdot 2H_2O$) in 2-methoxyethanol. The solutions were stirred for 2 hours at 65°C prior to combination to obtain weight ratios of (ZnO-SnO_2) of (10-90), (20-80), (30-70), and (40-60). Pure SnO_2, pure ZnO, and the 50:50 ZnO-SnO_2 composition were not synthesized, we focused on asymmetric ratios to probe synergistic effects beyond well-studied pure and equimolar cases. Monoethanolamine (MEA) was subsequently added dropwise to the solution as a stabilizer. The mixture was stirred at 30°C for 40 minutes. The mixture was heated to 70°C, stirred for 2 hours, and subsequently filtered through a paper filter to eliminate impurities. The final solutions were subjected to a 24-hours aging period at room temperature to achieve homogeneity. The quartz substrates underwent pre-cleaning in an ultrasonic bath with acetone, ethanol, methanol, and deionized water for 20 minutes each. The precursor solutions were spin-coated onto the cleaned substrates at 3400 rpm for 30 seconds. The spin-coated films were dried on a hot plate at 250°C for 15 minutes. The process was repeated eight times to attain the specified film

thickness. The final films were post-annealed at 350°C for 2 hours to eliminate solvents and organic residuals. The synthesis was conducted for each ZnO to SnO_2 ratio, yielding thin films designated as SZ1, SZ2, SZ3, and SZ4 for the (10-90), (20-80), (30-70), and (40-60) wt.% compositions, respectively.

3 RESULTS AND DISCUSSION

3.1 XRD Analysis

Since "Zinc tin oxide/zinc stannate occur in two individual oxides with distinct crystal structures and varying Zn/Sn ratios. These oxides are known as orthorhombic or perovskite $ZnSnO_3$ and cubic spinel-type Zn_2SnO_4 Based on the available data, Zn2SnO4 demonstrates higher thermal stability compared to $ZnSnO_3$. Zn_2SnO_4 possesses a cubic spinel arrangement, which has been previously established as the most thermodynamically stable form. Alternatively, $ZnSnO_3$ is formed under non-equilibrium conditions, such as high pressure, suggesting its thermodynamic metastability as a crystal phase. The formation of metastable $ZnSnO_3$ requires high pressure and energy conditions. The phase transition from metastannate to orthostannate begins at approximately 500 °C, with an activation energy of around 0.965 eV. Subsequently, recrystallization occurs, leading to the formation of the orthostannate phase with an inverse spinel structure, which is typically observed at around 750 °C. This investigation provides valuable insights into the behaviour of perovskite $ZnSnO_3$ undergoing a phase change to inverse spinel Zn_2SnO_4 during calcination" [1]. In this work, as shown in Figure 1, the X-ray diffraction patterns of $ZnSnO_3$ thin films emphasize their polycrystalline characteristics. The 2θ values of the XRD peaks for SZ1 align accurately with the tetragonal crystallite structure of SnO_2. The XRD patterns indicate that all angles are within the range of (10° to 80°), with the most prominent peaks observed at approximately 26° and 33°, which correspond to the (110) and (101) planes, respectively. According to standard values for tin oxide "(ICSD card: 01-077-0451)"[20], [21], and zinc stannate "(ICSD card: 98-002-4195)", the most significant peaks are illustrated in Figure 1. The thin films exhibit preferential orientations along the (110) and (101) planes. The peak intensity diminishes as the Zn ratio increases relative to the Sn ratios, which influence these preferred orientations. The crystal structure shows enhanced peak broadening and the presence of additional peaks in the XRD pattern associated with hexagonal zinc stannate "(ICSD: 98-002-4195)"[22]. This phenomenon results from the increased incorporated Zn^{2+} ions into the Sn oxide matrix. Prior research on SnO2 films with zinc incorporation has consistently shown analogous results concerning the preferred orientation behavior of the ($ZnSnO_3$) thin films [22], [23]. Figure 2 illustrates the reduction in crystallite size as Zn content increases in the ($ZnSnO_3$) matrix, as determined by the Halder-Wagner model, which demonstrates superior accuracy relative to other models in the context of noisy materials. All the equations and all other parameters utilized for detemining "crystallite sizes through various methods, including Scherrer's, Munshi-Scherer's, Williamson-Hall's, and Halder-Wagner's, as presented in our recent publications"[7], [24].

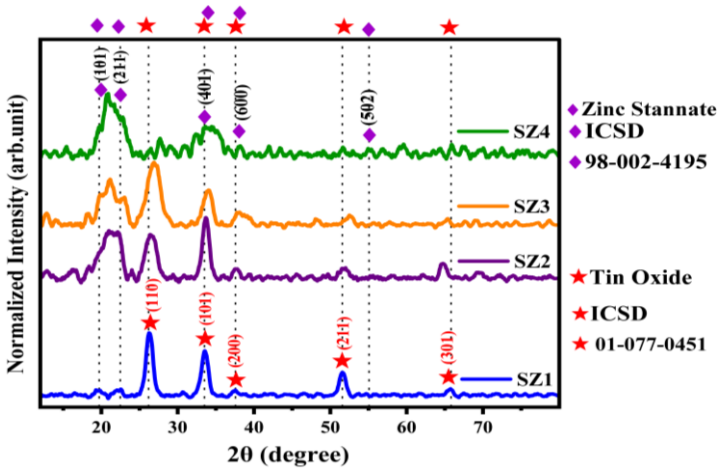

Figure 1: Normalized XRD pattern for $ZnSnO_3$ thin films at ratios of (10:90), (20:80), (30:70), and (40:60) wt.% (Zn-Sn), labeled as SZ1, SZ2, SZ3, and SZ4, respectively.

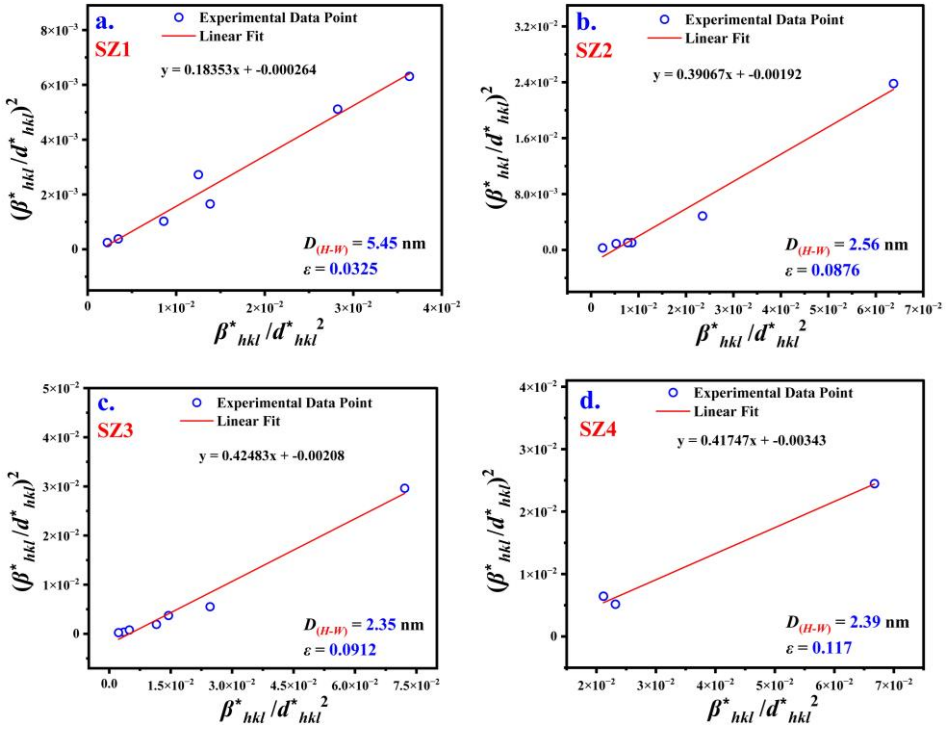

Figure 2: XRD patterns for (10:90), (20:80), (30:70), and (40:60) wt.% (ZnO-SnO_2) coated films annealed at 350°C, designated as SZ1, SZ2, SZ3, and SZ4, respectively, using the Halder-Wagner model.

4 MORPHOLOGICAL AND ELEMENTAL INSIGHTS

The surface morphology of the coated films was examined through FESEM imaging. The images demonstrate almost uniform distribution of small grains on the film surface, with no visible cracks present. The average crystallite size derived from the XRD diffraction, as presented in Figures 1 and 2, aligns with the results found from FESEM, depicted in Figure 3. The coated thin film demonstrates well-aligned top and cross-sectional surfaces, exhibiting excellent adhesion to the quartz (SiO2) substrates. Figure 5 clearly demonstrates that all oxide films possess a distinctly characteristic porous structure. Figures 3 (a-f) illustrate the complex morphology of the $ZnSnO_3$ film, demonstrating grains that approximate spherical shapes. The grain size of the SZ4 film, approximately 99 nm, exceeds that of the SZ1 film (33 nm), the SZ2 film (22 nm), and the SZ3 film (46 nm). This leads to a reduced grain size and increased porosity, subsequently resulting in an expanded surface area for oxygen's adsorption and test gas. Analyzing the differences in grain size among these films enhances our understanding of their structural properties [25], [26]. An efficient method for determining the composition and distribution of SZ1-4 nano-structured films is investigated through EDS mapping tests. Possible applications in gas sensing can benefit from the features enabled by the even distribution of Zn, Sn, and O. [27], [28]. This emphasizes the importance of strengthening analytics-driven synthesis methods to boost these materials' performance [29]. The elemental composition of the prepared films of each material corresponds to the samples labeled SZ1, SZ2, SZ3, and SZ4, respectively, with atomic percentages of (10:90), (20:80), (30:70), and (40:60) wt.% (ZnO-SnO_2) as shown in Figure 4. Element mapping was used to examine the thin films, which showed that Zn, Sn, and O were present and distributed uniformly throughout. Additional peaks indicating impurities were not found. Results showed that the stoichiometric quantity of Sn in samples deposited using (ZnO-SnO_2) was higher than Zn. The produced thin films' quality is greatly affected by surface roughness. Gas detection performance is also significantly impacted by factors like homogeneity and porosity. The efficiency of electron transport is improved when the surface is roughened because there are more active areas for interaction with reducing or oxidizing gases [26]. Atomic force

microscopy (AFM) was used to examine the surface morphology of the thin films that were produced. In Figure 5, images captured using 5 µm × 5 µm tapping mode scans are shown in both two-dimensional and three-dimensional formats, demonstrating the uneven but consistent formation of thin layers on the quartz base. Table 1 displays the values for the several roughness metrics, including the average roughness (Ra), root mean square (RMS) roughness (Rq), peak-to-valley roughness (Rt), skewness (Rsk), and kurtosis (Rku). The gas-sensing capabilities of $ZnSnO_3$ films are influenced by their topographical features, which are indicated by the surface roughness parameters Ra, Rq, and Rt. The increased gas molecule sensitivity is a result of the large surface area with many active sites shown by the elevated RMS roughness values of 47.8 and 36.7 in SZ2 and SZ3, respectively[30], [31]. Due to the presence of positive skewness (Rsk) values, the surface of the nanoparticle displays peaks rather than troughs. Gas retention and reduced interaction reaction time between the surface and the chemo-resistive layer may be aided by this property [32]. Also, a consistent and repeatable sensing response is the outcome of a rough distribution with increased sharp features, as shown by positive kurtosis (Rku) values [33]-[35]. The gas adsorption kinetics are increased by the combined surface characteristics, which in turn improve the sensitivity and response time of the sensor[32]-[34].

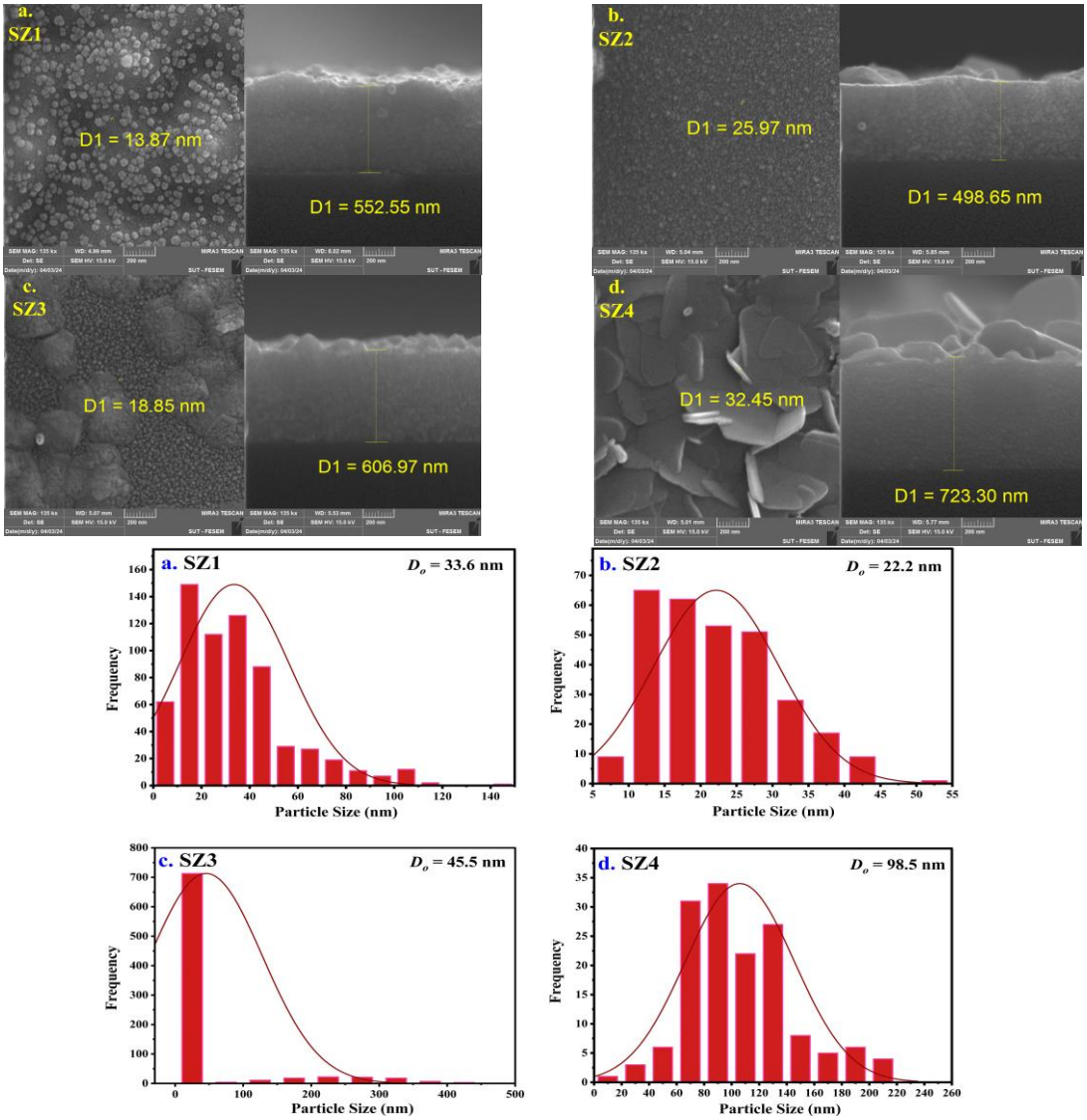

Figure 3: Histogram distribution for spin-coated films annealed at 350 °C, designated as: a) SZ1, b) SZ2, c) SZ3, d) SZ4, respectively.

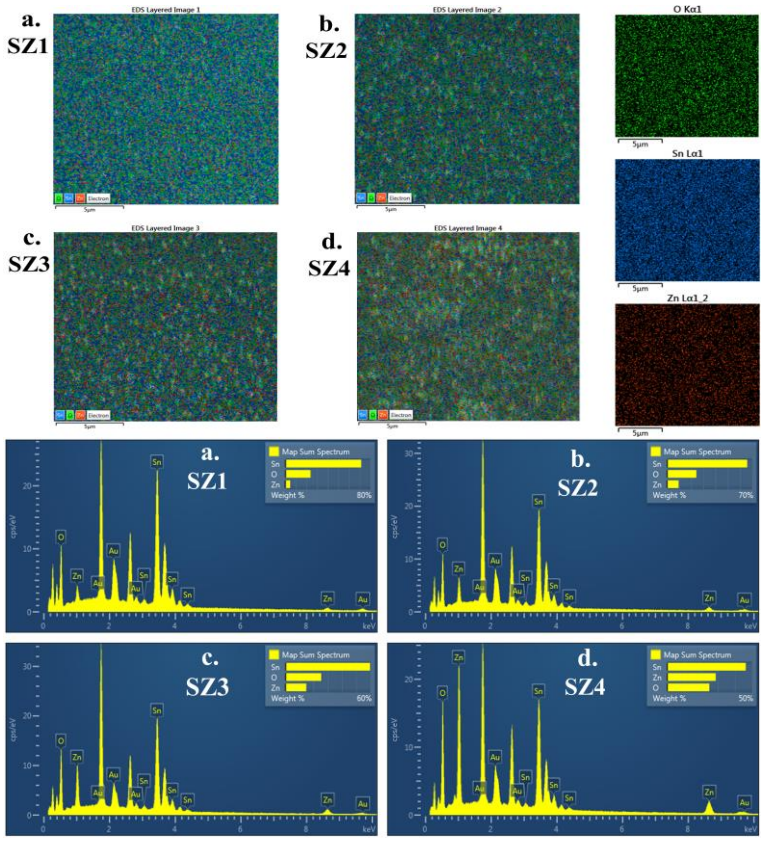

Figure 4: EDS mapping images of O, Sn, Zn for: a) SZ1,b) SZ2, c) SZ3, d) SZ4 thin films.

Table 1: AFM parameters' results for $ZnSnO_3$ films deposited at weight wt.% mixing ratios of (10:90), (20:80), (30:70), and (40:60) labeled as SZ1, SZ2, SZ3, and SZ4, respectively.

Sample Name	Roughness (*Ra*) (nm)	RMS *(Rq)* (nm)	Peak-to-Valley Roughness (Rt)(nm)	Skewness (Rsk)	kurtosis (Rku)
SZ1	27.5	34	294.2	0.4709	-0.7584
SZ2	38.3	47.8	453.8	0.6423	-0.5132
SZ3	29.6	36.7	346.0	0.6302	-0.5581
SZ4	11.7	14.9	104.4	0.7523	-0.4678

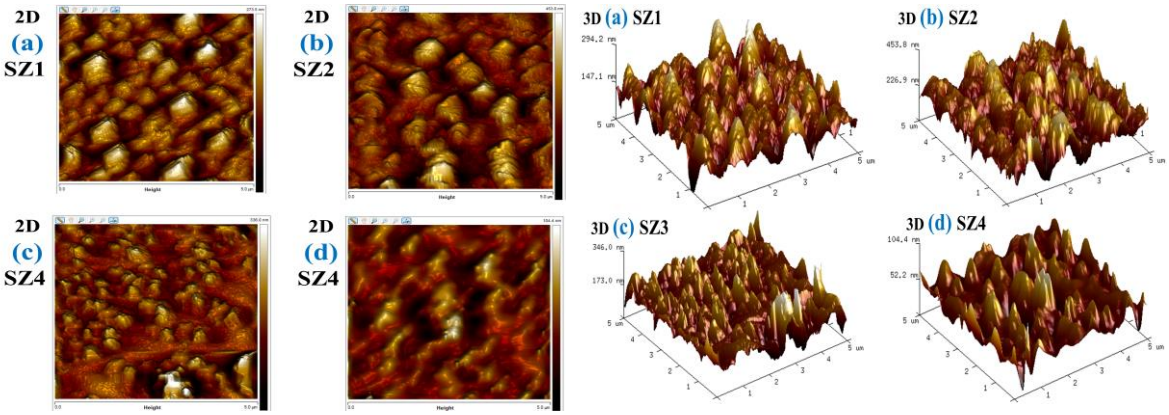

Figure 5: 2-D + 3-D AFM images for SZ1, SZ2, SZ3, and SZ4.

5 X-RAY PHOTOELECTRON SPECTROSCOPY (XPS)

In this part, XPS was used to examine the SZ1-4 films' surface elemental chemical structure. See the emissions of Sn, Zn, O, and C components in Figure 6a of the entire XPS spectrum. Additional peaks corresponding to other elements were not detected. The carbon element's C 1s peak at 284.6 eV is used as a reference signal and sample holder to calibrate the binding energy scale of the produced samples [35], [36]. By manipulating the Zn 2p and Sn 3d peak locations, one may view a multi-junction that happens in the region where Zn and Sn interact, or the interaction between ZnO and SnO_2[36]. By using peak fitting using Lorentzian and Gaussian to deconvolute the spectra of films coated with SZ1-4, the very precise spin-orbital splitting of Sn 3d can be shown in Figure 6b. The presence of Sn4+ ion-species in ZnSnO3 films is indicated by the binding energies of the Sn 3d5/2 peak at 486.15eV and the Sn 3d3/2 peak at 494.56eV. According to the typical spectra of Sn+4, there is an 8.41 eV binding-energy difference between $Sn3d^{3/2}$ and $Sn3d^{5/2}$[35], [37]. Figure 6c of the Zn2p spectra shows symmetric peaks at 1044.55 eV and 1021.46 eV, which correspond to the spin-orbital splitting of $Zn2p^{1/2}$ and $Zn2p^{3/2}$, respectively. Zn is present in its usual oxidation state of Zn^{2+}, as shown by the 23.09 eV binding energy difference between $Zn2p^{1/2}$ and $Zn2p^{3/2+}$[38], [39]. Based on the observed binding energy, the asymmetrical character of the oxygen high-resolution spectrum suggests numerous chemical states. Deconvoluting the O1s peak yields two Voigt fit peaks at 531.91 eV and 530.00 eV, which are the lattice oxygen in ZnO and SnO_2, respectively [36] (Fig. 6d). It is believed that oxygen vacancies and Zn-O bonding are responsible for the higher binding energy peak (OII) at 531.91eV. On the other hand, narrowly attributing this property to oxygen vacancies is controversial and often points to the existence of -OH/chemisorbed (OI) species or oxygen vacancies in environments rich with defects [35], [40]. As the oxidation level increases, the oxygen lattice and vacancy intensities (XPS) and interlayer spacing (XRD) show progressive alterations.

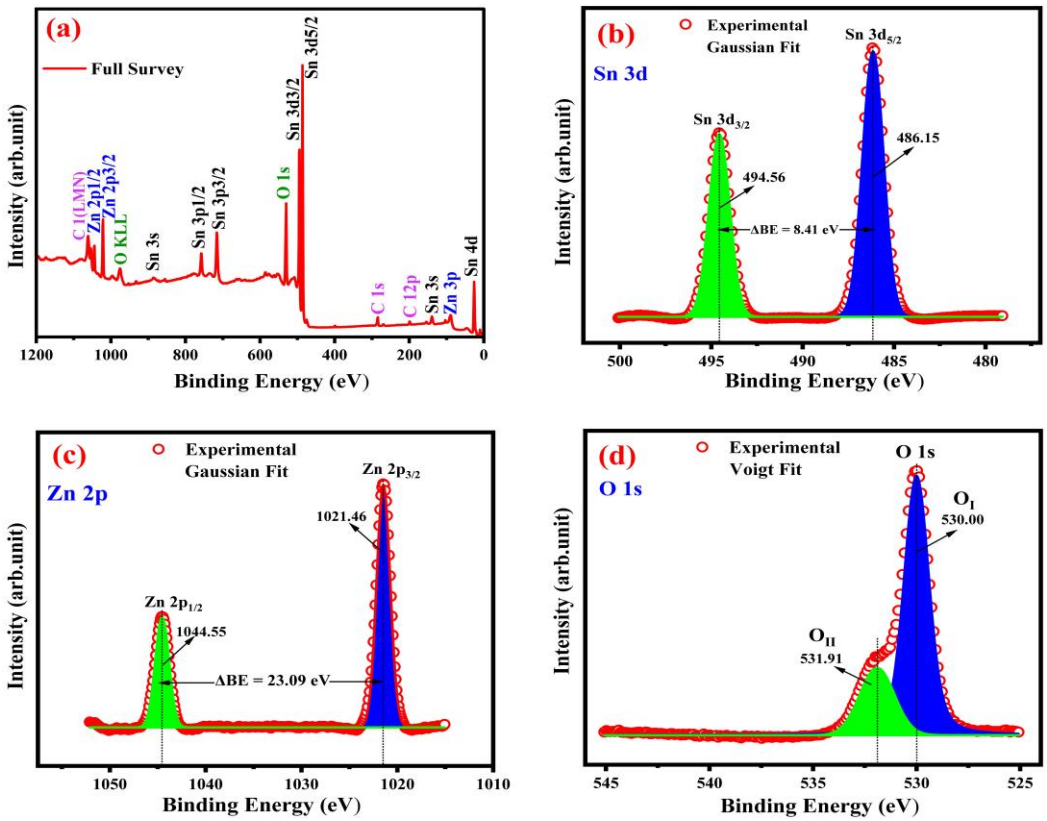

Figure 6: XPS spectra of $ZnSnO_3$ films annealed at 350 °C: a) "XPS full survey", b) "Sn 3d spectra", c) "Zn 2p spectra", d) "O 1s spectra".

6 RAMAN SPECTRUM

In Figure 7, an inset shows the Raman spectra of films made of $ZnSnO_3$ on quartz substrates with different weight (wt%) percentages of ZnO-SnO_2 annealed at 350 °C. The films are labeled SZ1, SZ2, SZ3, and SZ4, respectively. In order to detect trace amounts of oxides, Raman spectra have shown to be more effective than XRD studies. It may detect flaws, such as oxygen vacancies, and describe microstructural features [41]. A number of new physical phenomena in thin films may be better understood using this method [42]. According to the results of the previous XRD investigation, the structural characteristics and size changes of the crystallites are responsible for the differences in the intensity of the Raman peaks, which are shown as an inset in Figure 7. To gain better precision in Raman line location, spectra acquired from samples were fit using a deconvolution algorithm. The lines in Figure 7a, b, c and d show the cumulative fit to the data within the spectral range, which demonstrates this. There are noticeable bands at wavenumbers 200-800 cm^{-1} in the Raman spectra of the thin films that were deposited. It is possible that the quartz substrate and vibrations related to the tin-oxygen (Sn-O) stretching mode are responsible for the peaks seen between 500 cm^{-1} and 680 cm^{-1}[43]. The 690-788 cm^{-1} frequency range is associated with phonon modes in the O-Sn-O vibrational mode[44], [45]. One of the most noticeable peaks, located between 339 cm^{-1} and 500 cm^{-1}, corresponds to the E_2 high phonon mode, which is linked to stretching vibrations of ZnO. The E_1 (LO) Zn-O phonon mode, on the other hand, is associated with longitudinal optical phonons and has a lower intensity than the E_2 mode, it is often caused by (O-O) stretching and bending modes[46], [47]. Possible causes for the peaks seen below 263.74 cm^{-1} include free carriers, zinc interstitial or substitutional defect states, and oxygen vacancies [47]. “Raman spectra of Ag NP doped ZnO thin films were analyzed by Kamil et al., who found phonon modes, vibration modes, optical branches (both transverse and longitudinal), and optical branches (both positive and negative). As the amount of Ag NPs increases, the crystal quality declines, leading to oxygen vacancies, zinc interstitial defect states, free carriers, and a widening of the longitudinal optical peak. The phonon mode is responsible for the 420 cm^{-1} peak” . To determine whether $ZnSnO_3$ caused the change, “the CASTEP module of Materials Studio ran Raman spectra simulations. "The ilmenite (IL)-type structure (space group R3) and the LN-type structure (space group R3care the two known crystalline structures of zinc stannate ($ZnSnO_3$). In contrast to the latter, which was produced by solid-state reactions subjected to elevated temperatures and pressure, the former was ascertained by use of ion-exchange reactions [48], while the latter was synthesized via solid-state reactions under high pressure and raised temperature” [49]. The possibility of “IL-type and LN-type $ZnSnO_3$ coexisting at zero pressure was suggested by first-principles calculations carried out by Gou et al. In this investigation, the Raman spectra of $ZnSnO_3$ of the IL and LN types were modelled. Using the matching vibrational modes and the Raman shifts associated with them, the simulated Raman-shift peak spectra were labeled” [50]. With a Lorentzian smearing of 10 cm^{-1}, the coated samples SZ1-4 observed Raman spectra closely approach the simulated spectra of “IL-type” and “LN-type zinc stannate” (Zn-SnO_3).

7 OPTICAL PROPERTIES

Using UV-Visible absorption spectroscopy, the band gap of the produced SZ1-4 ZnSnO3 thin films was examined at different weight mixing ratios. Between 200 and 1100 nm, the absorption spectrum exhibits an exponential drop as the wavelength increases. All curves with lively contours suggest regular deposition. The refractive index and film thickness at two sites affect the distance between repeated vertices, which makes the samples different from each other [51]. The absorption spectra and Tauc’s plots of the synthesized SZ1-4 thin films are shown in Figure 8. To determine the optical bandgap of the nanostructures, the Tauc’s relation, as shown in (1), was used.

$$(\alpha h\nu)^2 = A(h\nu - E_g)^n. \quad (1)$$

The energy-independent constant A is used in this context, together with the optical bandgap energy Eg, the input photon energy hv, and the absorption coefficient α [52]. Figure 8 shows that Eg may be calculated by projecting the straight part of the curve onto the x-axis (hv). Band gap energies of 3.3, 3.36, 3.4, and 3.6 eV were determined for $ZnSnO_3$ thin films with Zn-Sn ratios of (10:90), (20:80), (30:70), and (40:60) wt.% (Zn-Sn), respectively, and designated as SZ1, SZ2, SZ3, and SZ4, respectively. All of these values are in agreement with what is stated in the literature [53]-[55]. As the mixing ratio increases, the bandgap widens because the quantum confinement effect is induced by the smaller crystallites [53], [54].

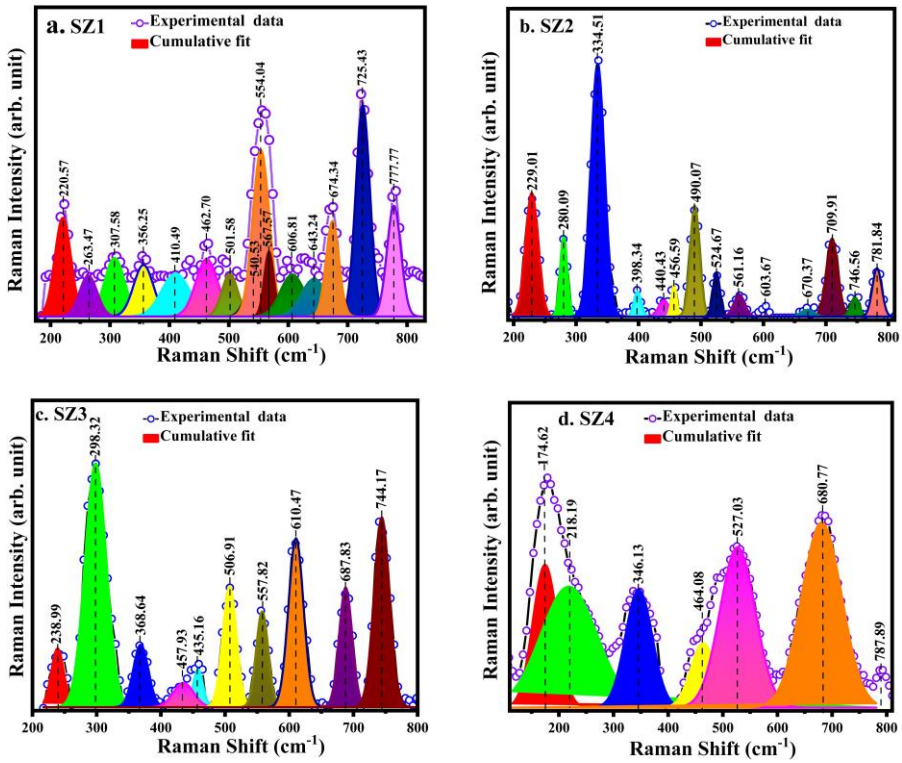

Figure 7: Raman spectra for: a) SZ1, b) SZ2, c) SZ3, d) SZ4 films annealed at 350 °C.

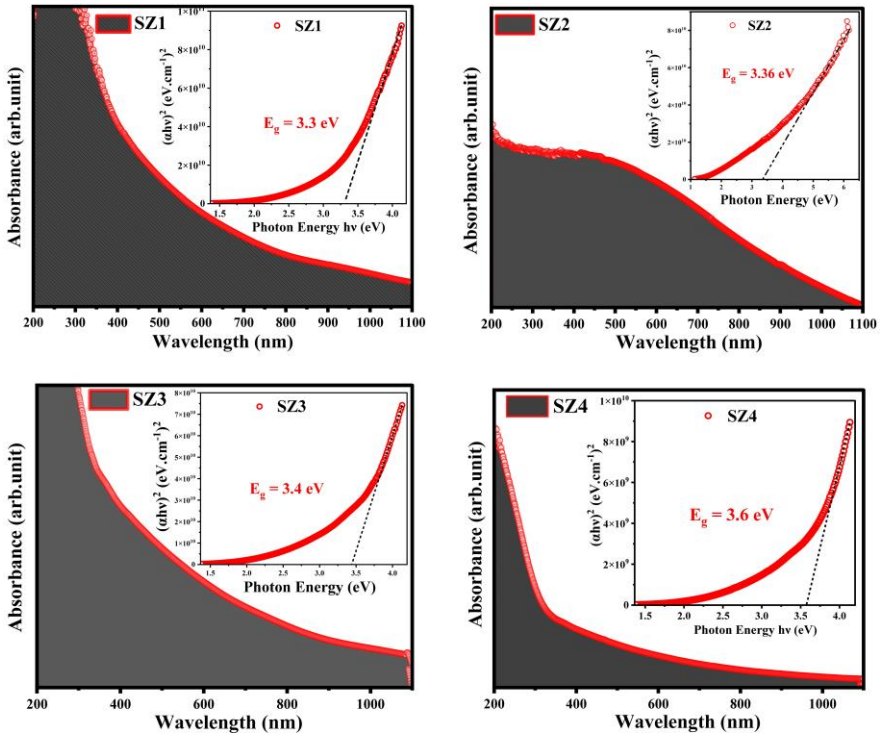

Figure 8: Absorption's spectra with Tauc's plot to determine the bandgap for SZ1, SZ2, SZ3, and SZ4 films.

Table 2: The Hall Effect measurements for SZ1, SZ2, SZ3, and SZ4 thin films.

Name of the Sample	Conductivity σ $(\Omega.cm)^{-1}$	Carriers Concentration n $(cm)^{-3}$	Resistivity $\boldsymbol{\rho}$ $(\Omega.\mathbf{cm})$	Mobility $\boldsymbol{\mu}$ (cm^2/Vs)
SZ1	1.97	6.22×10^{15}	5.07×10^{-1}	1.98×10^{3}
SZ2	1.87	5.82×10^{15}	5.34×10^{-1}	2.01×10^{3}
SZ3	2.11	8.11×10^{15}	4.73×10^{-1}	1.63×10^{3}
SZ4	3.37	1.24×10^{16}	2.97×10^{-1}	1.69×10^{3}

8 ELECTRIC PROPERTIES

A superb demonstration of the characteristics of semiconductor conduction is provided by investigating the Hall Effect of thin films, which reveals the type of majority charge carriers, their density, and their mobility. By measuring the Hall Effect, we confirmed that all the created films were n-type. Table 2 shows that when the Zn wt% mixing percentage rose, conductivity also increased. The rise in conductivity is due to the substitutional flaws in the lattice, which cause an increase in carrier concentration [56]. The changes in charge carrier mobility might be caused by changes in grain boundaries, which are a result of smaller crystallites when the Zn wt% increases relative to the Sn wt%. The presence of structural flaws, such as interstitials and oxygen and zinc vacancies, is responsible for this behavior because they alter the concentration of charge carriers. The semiconducting behavior is aided by oxygen interstitial atoms and zinc point defect vacancies, on the other hand, n-type behavior is produced by oxygen vacancies, which donate electrons. At a Zn concentration of 60 wt%, the electrical conductivity (σ) of the SZ1-4 thin films reaches a maximum of 3.37 Ω cm^{-1}, also known as SZ4, and a carrier concentration (n) of 1.24 × 10^16 cm^-3. According to earlier studies on the binary oxide (ZnO-SnO_2), illuminated-type $ZnSnO_3$ often has a better electrical conductivity than inverse spinel-type Zn_2SnO_4[1], [57], [58]. The films' Hall mobility shows no continuous pattern since it fluctuates with the mixing ratio. Carriers are unable to travel efficiently across bands due to the increased disorder inside the thin layers.

9 GAS SENSOR RESULTS

The low operating temperature of semiconductor gas sensors is one of their most prominent features. To get the operating temperature as low as feasible, researchers looked at how temperature affected the sensitivity of the spin-coated sheets. In order to study the changes in resistance over time, sensitivity, response, and recovery times for the spin-coated quartz substrates containing (10-90), (20-80), (30-70), and (40-60) wt.% (ZnO-SnO_2) thin films, the prepared films were subjected to NO_2, NH_3, and H_2S gases through an on-and-off gas switch. Temperatures ranging from 30 to 200 °C were used in the experiment. The sensor's active surface takes in oxygen molecules from the air around it. After that, electrons are removed from the conduction band of the sample surface, causing these molecules to become ionized. This process creates a surface depletion layer and several forms of oxygen ions[59]. The depletion layer's depth is proportional to the quantity of adsorbed gases. This layer might act as a barrier, blocking the channels between nearby nanoparticles and thereby preventing charge carriers from passing through. Contact with oxidizing gases reduces the mobility and concentration of charge carriers because they remove electrons from sample surfaces. This interaction modifies the thickness of the surface depletion layers. An increase in the sample's resistance is seen upon exposure to oxidizing fumes [60]. As a function of time, the resistance changes when exposed to NO_2, H_2S, and NH_3 gases at concentrations of 80 (ppm), 13 (ppm), and 11 (ppm), respectively. The resistance increases when the gas switch is opened. The resistance rapidly decreases with the depletion of NO_2 due to the gas's oxidizing properties. When decreased H_2S and NH_3 gases are used, however, the resistance behavior is the polar opposite. To find the sensitivity of the reducing and oxidizing gas sensors, we employed the computing approach outlined in the reference [61] in conjunction with (2) and (3).

$$S = \left|\frac{Rg - Ra}{Ra}\right| \times 100\% \quad \text{[Oxidizing gas]}, \quad (2)$$

$$S = \left|\frac{Rg - Ra}{Ra}\right| \times 100\% \quad \text{[Reducing gas]}. \quad (3)$$

Where the symbols Ra and Rg represent the film's resistance when exposed to air and gas, respectively, while S stands for sensitivity [62], the experiment used goal gases NO_2, H_2S, and NH_3 at constant concentrations. For NO_2, H_2S, and NH_3, the gas

sensitivity of $ZnSnO_3$ thin-film samples coated with spin-offs is shown in Figures 9a, b and c, respectively. When NO_2, H_2S, and NH_3 gases are present, the sensitivity is shown versus the operating temperature. Differences in sensitivity at various temperatures are caused by the different types and amounts of oxygen absorbed by the samples' surfaces. These oxygen species play a crucial role in the gas sensitivity processes. At 200 °C for NO2 and H_2S gases, and at RT (30 oC for NH_3), the $ZnSnO_3$ samples were most sensitive, respectively. The deposition conditions greatly affect the gas sensitivity of thin films, which is in line with previous research. Since there is a better chance of electrons reaching the electrode without recombining with defects when carrier mobility and diffusion length are both increased, gas sensitivity is enhanced [63]. Two potential reasons for this might be the grain-surface interaction or the roughness of the sample surfaces. In addition, the presence of oxygen vacancies is a crucial component that affects the sensitivity of the samples.

The reaction time of a gas sensor is the duration it takes for the conductance to reach 90% of its maximum or minimum value, respectively, when an oxidizing or reducing gas is added. This is shown by (4). Similarly, according to (5) [64], the recovery time is the time required for the sensor's resistance to return to about 10% of its original value once the gas flow is off.

$$\text{Response Time} = \left|t_{\text{gas (on)}} - t_{\text{gas (off)}}\right| \times 0.9, \quad (4)$$

$$\text{Recovery time} = \left|t_{\text{gas (off)}} - t_{\text{gas (recovery)}}\right| \times 0.9. \quad (5)$$

The recovery time and response time of ZnSnO3 thin films are shown in Figures 10a, b and c, Figure 11a, b and c for NO_2, H_2S, and NH_3, respectively, at operating temperatures of 30, 100, and 200 °C. In contrast to H_2S gas (19.8 seconds), NH_3 gas (54.9 seconds), and 53.1 seconds, respectively, NO_2 gas reacts rapidly (17.1 seconds) and recovers in 54.9 seconds, according to the graph. This demonstrates that the NO_2, H_2S, and NH_3 gas sensors react rapidly when the gas concentration is sufficient to trigger the desired response. The desorption process mostly causes a longer recovery time compared to the response time in gas detectors. Atoms of the target gas are assimilated into the detector's surface when a response is triggered, altering the device's electrical properties. However, desorption, the process by which the sensor returns to its original state once the gas has evaporated, takes time[65], [66].

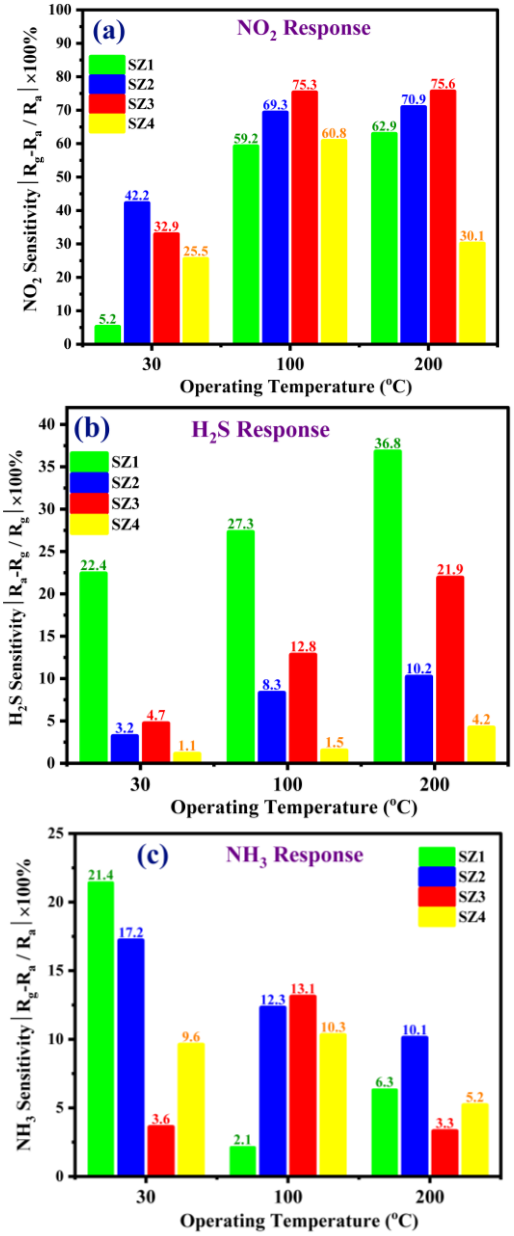

Figures 9: Sensitivity of $ZnSnO_3$ films: a) NO_2, b) H_2S, c) NH_3.

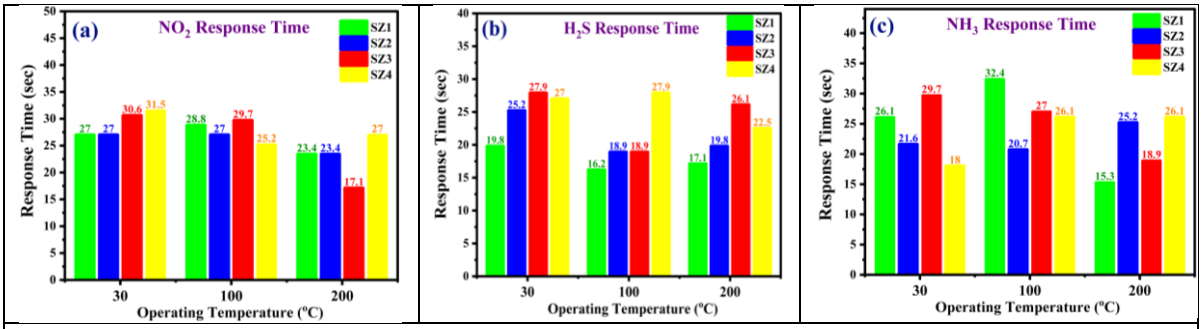

Figures 10: Response time of $ZnSnO_3$ films: a) NO_2, b) H_2S, c) NH_3.

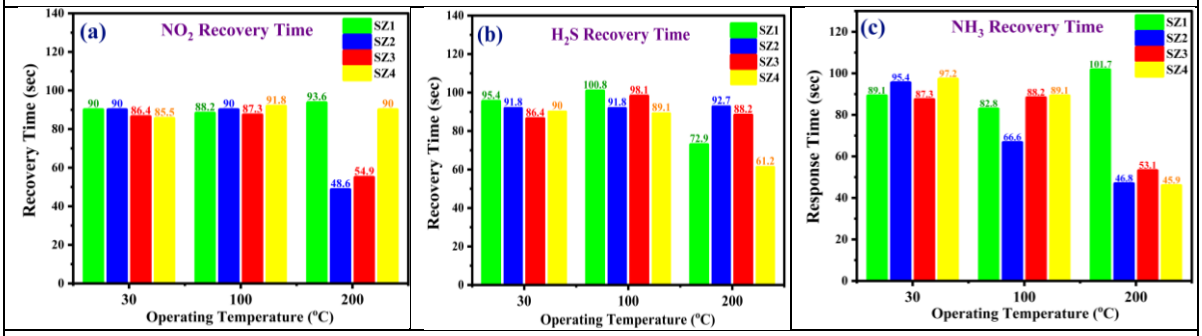

Figures 11: Recovery time of $ZnSnO_3$ films: a) NO_2, b) H_2S, c) NH_3.

10 CONCLUSIONS

This research presents the synthesis of ZnSnO3 films via the Sol-gel method, employing spin coating for deposition, and optimized for gas sensing applications, especially for detecting NO2, H2S, and NH3 gases. Optimizing the weight (wt%) ratios of ZnO and SnO enhanced gas sensing capabilities, with the thin films demonstrating favorable response and rapid response and recovery times. A variety of characterization techniques are conducted to calculate the structural, optical, electrical, and sensing characteristics of the synthesized thin films. The techniques encompass X-ray diffraction (XRD), X-ray photoelectron spectroscopy (XPS), Raman spectroscopy, atomic force microscopy (AFM), field-emission scanning electron microscopy (FE-SEM), energy-dispersive X-ray spectroscopy (EDS), UV-vis measurements, Hall Effect measurements, and sensitivity measurements. Structural characterization verified a phase transition from tetragonal rutile to hexagonal ilmenite with increasing Zn (wt%) concentration. The presence of oxygen vacancies and oxide states of Sn4+, Zn2+, and O2− has been confirmed, which is significant for the development of the film's gas-sensing properties. The morphological properties of the thin films, analyzed through FE-SEM and AFM tests, exhibited high RMS roughness values and nearly spherical nanostructures. These characteristics enhance the surface area, facilitating efficient gas adsorption and desorption processes. Optical measurements revealed band gaps between 3.3 and 3.6 eV, with a corresponding increase in electrical conductivity linked to improved sensing performance. The best response was obtained for ZnO:SnO_2 = 70:30 (wt%), delivering ~76% NO_2 sensitivity at 200 °C with a ~17 s response (LOD ≈ 81 ppm. The sensitivity values indicated that the prepared thin films effectively detect NO2, H2S, and NH3 at room temperature (RT), with notable improvements in response (S%) at elevated temperatures of 100°C and 200°C. The response times for these gases were swift, with the films indicating response times between 17 and 27 seconds, contingent upon the gas type and temperature. The results indicate that porous ZnSnO3 thin films are viable candidates for hazardous gas detection, with potential applications in environmental monitoring and industrial safety. The improved gas sensing performance, along with high sensitivity and quick response times, highlights the relevance of these films in practical gas detection applications, advancing gas sensor technology.

ACKNOWLEDGMENTS

The authors would like to express their sincere gratitude to the Department of Physics, College of Science, University of Diyala, for their continuous support and provision of the necessary facilities to conduct this research. The authors also extend their appreciation to all colleagues and technical staff whose guidance and assistance contributed to the successful completion of this study.

REFERENCES

[1] M. Rahman, M. S. Bashar, M. L. Rahman, and F. I. Chowdhury, "Comprehensive review of micro/nanostructured ZnSnO3: characteristics, synthesis, and diverse applications," RSC Advances, vol. 13, no. 44, pp. 30798-30837, 2023.

[2] A. Kumar, N. Sharma, A. P. Gutal, D. Kumar, P. Kumar, M. Paranjothy, and M. Kumar, "Growth and NO2 gas sensing mechanisms of vertically aligned 2D SnS2 flakes by CVD: Experimental and DFT studies," Sensors and Actuators B: Chemical, vol. 353, pp. 131078, 2022.

[3] S. K. Pandey, K.-H. Kim, and K.-T. Tang, "A review of sensor-based methods for monitoring hydrogen sulfide," TrAC Trends in Analytical Chemistry, vol. 32, pp. 87-99, 2012.

[4] Z. Aslam, I. A. Hussein, R. A. Shawabkeh, M. A. Parvez, W. Ahmad, and Ihsanullah, "Adsorption kinetics and modeling of H2S by treated waste oil fly ash," Journal of the Air & Waste Management Association, vol. 69, no. 2, pp. 246-257, 2019.

[5] C.-s. He, J.-c. Ye, H.-h. Zhang, X. Gong, and X. Li, "A review: Strategies for enhancing the performance of SnO2-based formaldehyde gas sensors," Microchemical Journal, vol. 208, pp. 112591, 2025.

[6] J. Park, D. Chaulagain, N. N. Same, A. O. Yakub, J. O. Lim, J. W. Roh, and J. S. Huh, "Formaldehyde gas response and selectivity of ZnO-SnO2 gas sensors," Sensors and Actuators B: Chemical, vol. 425, pp. 136958, 2025.

[7] K. S. Mohammed, J. ALzanganawee, and A. A. Kamil, "Optimizing ZnO-SnO2 thin-film ratios for high sensitivity to NO2 and NH3," Journal of Materials Science: Materials in Electronics, vol. 36, no. 22, pp. 1381, 2025.

[8] M. Wang, Q. Zeng, J. Cao, D. Chen, Y. Zhang, J. Liu, and P. Jia, "Highly sensitive gas sensor for detection of air decomposition pollutant (CO, NOx): popular metal oxide (ZnO, TiO2)-doped MoS2 surface," ACS Applied Materials & Interfaces, vol. 16, no. 3, pp. 3674-3684, 2024.

[9] B. Maji, P. Singh, and S. Badhulika, "A highly sensitive and fully flexible Fe-Co metal-organic framework hydrogel based gas sensor for ppb level detection of acetone," Applied Surface Science, vol. 678, pp. 161047, 2024.

[10] K. S. Mohammed, J. Al-Zanganawee, and A. A. Kamil, "Defect-Engineered Ni-Cu Co-Doped ZnO-SnO2 Thin-Film Ceramics by Sol-Gel Spin Coating for Selective, Fast Six-Gas Sensing (NO2, H2S, NH3, and VOCs) from Room Temperature to 200° C," Journal of Alloys and Compounds, pp. 184032, 2025.

[11] J. Ding, Z. Luo, Y. Sun, B. Ren, S. Fu, Y. Yang, J. Cui, X. Wang, and J. Yue, "A room temperature NO2 gas sensor based on Rb-doped ZnO/In2O3 nano-heterojunction with high performance," Journal of Alloys and Compounds, vol. 1003, pp. 175736, 2024.

[12] C. N. Wang, Y. L. Li, F. L. Gong, Y. H. Zhang, S. M. Fang, and H. L. Zhang, "Advances in doped ZnO nanostructures for gas sensor," The Chemical Record, vol. 20, no. 12, pp. 1553-1567, 2020.

[13] C. Liu, Q.-Q. Zou, B. Liu, and Y. Zhang, "A visible-light-assisted Pd/TiO2 gas sensor with carbon nanotubes electrodes for trace formaldehyde detection," Rare Metals, vol. 43, no. 1, pp. 257-266, 2024.

[14] R. Kumar, Mamta, R. Kumari, and V. N. Singh, "SnO2-based NO2 gas sensor with outstanding sensing performance at room temperature," Micromachines, vol. 14, no. 4, pp. 728, 2023.

[15] X. Li, L. Fu, H. Karimi-Maleh, F. Chen, and S. Zhao, "Innovations in WO3 gas sensors: Nanostructure engineering, functionalization, and future perspectives," Heliyon, vol. 10, no. 6, 2024.

[16] M. Zhang, X. Lv, T. Wang, W. Pei, Y. Yang, F. Li, D. Yin, H. Yu, and X. Dong, "CuO-based gas sensor decorated by polyoxometalates electron acceptors: From constructing heterostructure to improved sensitivity and fast response for ethanol detection," Sensors and Actuators B: Chemical, vol. 415, pp. 136016, 2024.

[17] K. S. Mohammed, J. ALzanganawee, and A. A. Kamil, "A novel approach to low-temperature gas sensing using sol-gel spin-coated (NiO: ZnO: SnO2) thin films for NO2, H2S, and NH3 detection," Journal of Sol-Gel Science and Technology, pp. 1-25, 2025.

[18] T. Chen, J. Sun, N. Xue, W. Wang, Z. Luo, Q. Liang, T. Zhou, H. Quan, H. Cai, and K. Tang, "Cu-doped SnO2/rGO nanocomposites for ultrasensitive H2S detection at low temperature," Microsystems & Nanoengineering, vol. 9, no. 1, pp. 69, 2023.

[19] K. S. Mohammed, J. M. M. Al-Zanganawee, and A. A. Kamil, "An investigation of (Co+ Zn) co-doping effect on certain physical features of nano-structured (CdO) thin films deposited by sol-gel spin coating technique," pp. 090004.

[20] G. Lamdhade, F. Raghuwanshi, R. Agrawal, V. Balkhande, and T. J. A. M. L. Shripath, "SnO2 nanoparticles synthesis via liquid-phase co-precipitation technique," vol. 6, pp. 738-742, 2015.

[21] S. Chen, Z. Sun, L. Zhang, and H. J. C. Xie, "Photodegradation of gas phase benzene by SnO2 nanoparticles by direct hole oxidation mechanism," vol. 10, no. 1, pp. 117, 2020.

[22] D. Redolfi-Bristol, L. Branzi, M. Back, P. Riello, A. Speghini, N. Pinna, and A. J. I. Benedetti, "ZnSnO3 or Zn2SnO4/SnO2 Hierarchical Material? Insight into the Formation of ZnSn(OH)6 Derived Oxides," vol. 10, no. 11, pp. 183, 2022.

[23] W. J. J. o. T. E. S. Guo, "Hollow and porous ZnSnO3 gas sensor for ethanol gas detection," vol. 163, no. 5, pp. B131, 2016.

[24] K. Mohammed, J. ALzanganawee, and A. A. Kamil, "A novel approach to low-temperature gas sensing using sol-gel spin-coated (NiO: ZnO: SnO2) thin films for NO2, H2S, and NH3 detection," Journal of Sol-Gel Science and Technology, pp. 1-25, 2025.

[25] S. Dabbabi, T. B. Nasr, A. Madouri, A. Cavanna, A. Garcia-Loureiro, and N. J. p. s. s. Kamoun, "Fabrication and characterization of sensitive room temperature NO2 gas sensor based on ZnSnO3 thin film," vol. 216, no. 16, pp. 1900205, 2019.

[26] Y. Shi, H. Xu, T. Liu, S. Zeb, Y. Nie, Y. Zhao, C. Qin, and X. J. M. A. Jiang, "Advanced development of metal oxide nanomaterials for H2 gas sensing applications," vol. 2, no. 5, pp. 1530-1569, 2021.

[27] M. V. Nikolic, V. Milovanovic, Z. Z. Vasiljevic, and Z. J. S. Stamenkovic, "Semiconductor gas sensors: Materials, technology, design, and application," vol. 20, no. 22, pp. 6694, 2020.

[28] Y.-F. Sun, S.-B. Liu, F.-L. Meng, J.-Y. Liu, Z. Jin, L.-T. Kong, and J.-H. J. S. Liu, "Metal oxide nanostructures and their gas sensing properties: a review," vol. 12, no. 3, pp. 2610-2631, 2012.

[29] G. J. C. a. Korotcenkov, "Handbook of gas sensor materials," vol. 1, 2013.

[30] R. Shrivastava, and K. Singh, "Interlaminar fracture toughness characterization of laminated composites: a review," Polymer Reviews, vol. 60, no. 3, pp. 542-593, 2020.

[31] D. Y. Nadargi, A. Umar, J. D. Nadargi, S. A. Lokare, S. Akbar, I. S. Mulla, S. S. Suryavanshi, N. L. Bhandari, and M. G. Chaskar, "Gas sensors and factors influencing sensing mechanism with a special focus on MOS sensors," Journal of Materials Science, vol. 58, no. 2, pp. 559-582, 2023.

[32] S. Park, "Chemoresistive gas sensing properties of functionalized two-dimensional materials," M.S. thesis, Dept. Mater. Sci. Eng., Seoul National Univ., Seoul, South Korea, 2020.

[33] V. Bučinskas, A. Dzedzickis, E. Šutinys, and T. Lenkutis, "Implementation of different gas influence for operation of modified atomic force microscope sensor," Solid State Phenomena, vol. 260, pp. 99-104, 2017.

[34] D. Rajkumar, H. Umamahesvari, and P. Nagaraju, "Synthesis and characterization of anatase phase TiO2 thin films for formaldehyde detection," Journal of Materials Science: Materials in Electronics, vol. 35, no. 1, pp. 32, 2024.

[35] M. Chaskar, V. Kadam, C. Jagtap, N. Naik, H. Pathan, P. J. E. E. Adhyapak, and Environment, "Enhancement of Photovoltaic Performance of Dye-Sensitized Solar Cells Using Hierarchical Zinc Oxide/Tin Oxide (ZnO/SnO2) Nanocomposites Synthesized via Hydrothermal Method," vol. 26, pp. 1250, 2024.

[36] F. G. El Desouky, M. Saadeldin, W. H. J. S. Eisa, and Interfaces, "Synergistic influence of SnFe2O4 on ZnSnO3 hybrid nanostructures and optimizations optical, photoluminescence, and magnetic properties for multifunction application," vol. 38, pp. 102749, 2023.

[37] M. T. Uddin, Y. Nicolas, C. Olivier, T. Toupance, L. Servant, M. M. Muller, H.-J. Kleebe, J. Ziegler, and W. J. I. c. Jaegermann, "Nanostructured SnO2-ZnO heterojunction photocatalysts showing enhanced photocatalytic activity for the degradation of organic dyes," vol. 51, no. 14, pp. 7764-7773, 2012.

[38] S. Cynthia, R. Sivakumar, and C. J. O. Sanjeeviraja, "Ternary CuO: SnO2: ZnO (1:1:1) composite thin film for room temperature gas sensor application," vol. 234, pp. 166615, 2021.

[39] S. Chen, F. Liu, M. Xu, J. Yan, F. Zhang, W. Zhao, Z. Zhang, Z. Deng, J. Yun, R. J. J. o. c. Chen, and i. science, "First-principles calculations and experimental investigation on SnO2@ZnO heterojunction photocatalyst with enhanced photocatalytic performance," vol. 553, pp. 613-621, 2019.

[40] P. A. Hind, P. Kumar, U. K. Goutam, and B. V. Rajendra, "Impact of deposition temperature on persistent photoconductivity of SnO2 thin films deposited using spray pyrolysis technique suitable in optoelectronic synaptic devices," Optical Materials, vol. 153, 2024.

[41] F. G. El Desouky, I. Moussa, and M. J. I. J. o. P. Obaida, "UV photo-sensing performance of NiSnO3 thin films deposited by pulsed spray pyrolysis technique," pp. 1-13, 2024.

[42] C. Mrabet, M. B. Amor, A. Boukhachem, M. Amlouk, and T. J. C. I. Manoubi, "Physical properties of La-doped NiO sprayed thin films for optoelectronic and sensor applications," vol. 42, no. 5, pp. 5963-5978, 2016.

[43] X. Li, and C. J. R. a. Wang, "Significantly increased cycling performance of novel 'self-matrix' NiSnO3 anode in lithium ion battery application," vol. 2, no. 15, pp. 6150-6154, 2012.

[44] S. Mehraj, M. S. Ansari, A. A. J. M. C. Al-Ghamdi, and Physics, "Annealing dependent oxygen vacancies in SnO2 nanoparticles: Structural, electrical and their ferromagnetic behavior," vol. 171, pp. 109-118, 2016.

[45] P. Patil, R. Kawar, T. Seth, D. Amalnerkar, and P. J. C. I. Chigare, "Effect of substrate temperature on structural, electrical and optical properties of sprayed tin oxide (SnO2) thin films," vol. 29, no. 7, pp. 725-734, 2003.

[46] A. J. J. P. M. S. Khan, "Raman spectroscopic study of the ZnO nanostructures," vol. 4, no. 1, pp. 5-9, 2010.

[47] M. Šćepanović, M. Grujić-Brojčin, K. Vojisavljević, S. Bernik, and T. J. J. o. R. S. Srećković, "Raman study of structural disorder in ZnO nanopowders," vol. 41, no. 9, pp. 914-921, 2010.

[48] D. Kovacheva, and K. J. S. S. I. Petrov, "Preparation of crystalline ZnSnO3 from Li2SnO3 by low-temperature ion exchange," vol. 109, no. 3-4, pp. 327-332, 1998.

[49] Y. Inaguma, M. Yoshida, and T. J. J. o. t. A. C. S. Katsumata, "A polar oxide ZnSnO3 with a LiNbO3-type structure," vol. 130, no. 21, pp. 6704-6705, 2008.

[50] Q. Ge, C. Liu, Y. Zhao, N. Wang, X. Zhang, C. Feng, S. Zhang, H. Wang, W. Jiang, and S. J. A. P. A. Liu, "Phase evolution in preparing ZnSnO3 powders by precipitation method," vol. 127, pp. 1-8, 2021.

[51] K. Mohammed, J. Mansoor, J. Alzanganawee, and S. Iftimie, "An investigation of annealing and (Zn+Co) co-loading impact on certain physical features of nano-structured (CdO) thin films coated by a sol-gel spin coating process," Journal of Ovonic Research, vol. 17, no. 5, 2021.

[52] B. Abdallah, A. Jazmati, and M. J. O. Kakhia, "Physical, optical and sensing properties of sprayed zinc doped tin oxide films," vol. 158, pp. 1113-1122, 2018.

[53] M. O. S. Al-Gburi Dr, G. J. Habi, and N. J. J. K. I. J. o. M. S. Hentawe, "Effect of mixing ratio of (SnO2)1-x(In2O3)x thin film on gas sensitivity," vol. 6, no. 1, pp. 12, 2020.

[54] D. Meena, V. K. Verma, and S. J. M. T. P. Rana, "Investigation the effect of Zn doping on structural and optical properties of SnO2," vol. 51, pp. 554-560, 2022.

[55] Riahi, B. Khalfallah, F. J. O. Chaabouni, and Q. Electronics, "Physico-chemical properties of perovskite ZnSnO3 thin films deposited on glass and silicon wafers by RF magnetron sputtering," vol. 54, no. 8, pp. 514, 2022.

[56] S. Jin, Y. Yang, J. E. Medvedeva, J. R. Ireland, A. W. Metz, J. Ni, C. R. Kannewurf, A. J. Freeman, and T. J. Marks, "Dopant ion size and electronic structure effects on transparent conducting oxides. Sc-doped CdO thin films grown by MOCVD," Journal of the American Chemical Society, vol. 126, no. 42, pp. 13787-13793, 2004.

[57] H. W. Kim, E. Lee, D. Kim, S. Seong, S. Y. Moon, Y.-J. Shin, J. Baik, H. Shin, and J.-S. Kang, "Soft X-ray absorption and photoemission spectroscopy study of semiconductor oxide nanoparticles for dye-sensitized solar cell: ZnSnO3 and Zn2SnO4," Solid State Communications, vol. 236, pp. 32-36, 2016.

[58] L. Shi, and J. Ding, "Controlled synthesis and photocatalytic activity of Zn2SnO4 nanotubes and nanowires," Ceramics International, vol. 44, no. 12, pp. 14693-14697, 2018.

[59] A. Staerz, U. Weimar, and N. Barsan, "Current state of knowledge on the metal oxide based gas sensing mechanism," Sensors and Actuators B: Chemical, vol. 358, pp. 131531, 2022.

[60] J. Hsieh, C. Liu, and Y. Ju, "Response characteristics of lead phthalocyanine gas sensor: effects of film thickness and crystal morphology," Thin Solid Films, vol. 322, no. 1-2, pp. 98-103, 1998.

[61] L. A. Patil, A. R. Bari, M. D. Shinde, V. V. Deo, and D. P. Amalnerkar, "Synthesis of ZnO nanocrystalline powder from ultrasonic atomization technique, characterization, and its application in gas sensing," IEEE Sensors Journal, vol. 11, no. 4, pp. 939-946, 2010.

[62] L. Fan, X. Yang, and H. Sun, "A novel flexible sensor for double-parameter decoupling measurement of temperature and pressure with high sensitivity and wide range," Journal of Materials Chemistry C, vol. 11, no. 30, pp. 10163-10177, 2023.

[63] T. Maeda, and M. Sugiyama, "Controlling the structure and composition of SnO2-based thin film with reactive sputtering to improve the sensitivity of semiconductor CO2 sensor," Japanese Journal of Applied Physics, vol. 63, no. 4, pp. 045501, 2024.

[64] N. K. Abbas, I. M. Ibrahim, and M. A. Saleh, "Characteristics of MEH-PPV/Si and MEH-PPV/PS heterojunctions as NO2 gas sensors," Silicon, vol. 10, no. 4, pp. 1345-1350, 2018.

[65] S. Pagidi, K. S. Pasupuleti, M. Reddeppa, S. Ahn, Y. Kim, J.-H. Kim, M.-D. Kim, S. H. Lee, and M. Y. Jeon, "Resistive type NO2 gas sensing in polymer-dispersed liquid crystals with functionalized-carbon nanotubes dopant at room temperature," Sensors and Actuators B: Chemical, vol. 370, pp. 132482, 2022.

[66] M. V. Nikolic, V. Milovanovic, Z. Z. Vasiljevic, and Z. Stamenkovic, "Semiconductor gas sensors: Materials, technology, design, and application," Sensors, vol. 20, no. 22, pp. 6694, 2020, doi: 10.3390/s20226694.